Manuscript received March 6, 2013

Efficient Computation of the Coupling Between a Vertical Line Source and a Slot

Guido Valerio, *Member, IEEE*, Massimiliano Casaletti, *Member, IEEE*,
Josip Seljan, Ronan Sauleau, *Senior Member, IEEE*, and Matteo Albani, *Senior Member, IEEE*

***Abstract*—A novel spectral formulation is proposed here for the coupling integral between a cylindrical wave with arbitrary radial wavenumber and azimuthal dependence, and a slot placed on a plane orthogonal to the wavefront. Such a kind of integral is massively encountered in electromagnetic modeling of stratified structures comprising slots and vertical pins or vias. The two-fold spatial integral defining the coupling is transformed into an equivalent one-fold spectral integral, the integration path of which is selected to obtain Gaussian decay of the integrand. Both propagating and evanescent cylindrical modes are considered. An arbitrary stratification orthogonal to the slot plane can be considered, as well as an arbitrary current on the slot. Numerical comparisons against the standard spatial approach are shown to validate the new formulation, and its advantage in terms of computation cost is investigated in depth.**

***Index Terms*—Slot coupling, spectral methods, cylindrical waves, steepest descent path, numerical methods.**

I. Introduction

NUMERICAL modeling of arbitrarily-shaped slotted waveguides and antennas is a vast research topic receiving considerable attention in last years, as the degree of complexity of the analyzed structures increases and their fine details need to be correctly described [1],[2].

Integral-equation methods provide convenient tools to study these structures, since Green's functions for layered media can be rigorously determined [3]-[5], and slots can be replaced by equivalent unknown currents coupling different regions, solved through the method of moments (MoM). Various full-wave and approximate methods have been developed for the fast computation of slots couplings, based on Green's functions approximations or integral transforms [6]-[8].

A more difficult problem is the study of slotted structures involving vertical elements. They are lately becoming of wide interest, due to the development of substrate integrated waveguides (SIW), easily fabricated and integrated with printed circuits, e.g. [9]-[15]. These structures require the modelization of a large number of vertical vias, and can be handled conveniently by coupling a Mode Matching (MM) technique for the closed SIW structure [16] with a MoM solution for the slot currents [17]. A large number of integral coupling the cylindrical waves scattered by each posts with the slots must be computed, and the possibility to solve large slotted SIW is strictly depending on an efficient calculation of these integrals. A very large number of vertical posts is usually present, placed at moderate or large distances from each slot. The possibility to obtain a reliable and accelerated computation strategy for the interaction between largely-spaced slot and post is particularly useful.

No method has been proposed so far as an alternative to the simple twofold spatial integration over the slot region. In this paper rigorous alternative expressions are derived together with a discussion on their range of validity and the computational advantage we can expect to obtain.

The paper is organized as follows. In Section II, the spatial-domain coupling integral is transformed into an equivalent spectral integral, and the integration path is deformed into a steepest descent path (SDP) in order to grant a fast exponential decay of the integrand. In Section III, numerical results are provided to validate the analytical manipulations. The computational advantages of the proposed approach is also discussed as the physical and geometric parameters vary in range of practical interest.

II. Spectral-Domain Transformation

We address in this section the efficient computation of the integrals coupling a cylindrical wave centered at $\boldsymbol{\rho}_\mathrm{C}$ and the equivalent magnetic current $\mathbf{B}$ on a slot centered at $\boldsymbol{\rho}_\mathrm{S}$, lying on a plane orthogonal to the wavefront, as introduced in [17]:

$$R_n^{\mathrm{TM}}\left(\boldsymbol{\rho}_\mathrm{S}-\boldsymbol{\rho}_\mathrm{C},z;\kappa_\rho^{\mathrm{TM}}\right)=\int_S \mathbf{M}_n\left(\boldsymbol{\rho}-\boldsymbol{\rho}_\mathrm{C},z;\kappa_\rho^{\mathrm{TM}}\right)\cdot\mathbf{B}\left(\boldsymbol{\rho}-\boldsymbol{\rho}_\mathrm{S}\right)\mathrm{d}\boldsymbol{\rho} \quad (1)$$

and

$$R_n^{\mathrm{TE}}\left(\boldsymbol{\rho}_\mathrm{S}-\boldsymbol{\rho}_\mathrm{C},z;\kappa_\rho^{\mathrm{TE}}\right)=\int_S \mathbf{N}_n\left(\boldsymbol{\rho}-\boldsymbol{\rho}_\mathrm{C},z;\kappa_\rho^{\mathrm{TE}}\right)\cdot\mathbf{B}\left(\boldsymbol{\rho}-\boldsymbol{\rho}_\mathrm{S}\right)\mathrm{d}\boldsymbol{\rho} \quad .(2)$$

The $\boldsymbol{\rho}$ and z coordinates refer to the global reference system $(x_\mathrm{G}, y_\mathrm{G})$ in Fig. 1. $\kappa_\rho^{\mathrm{TM/TE}}$ is the radial wavenumber of a mode with TM or TE polarization with respect to the axis of the wavefront. $\mathbf{M}$ and $\mathbf{N}$ are cylindrical-wave vector functions [3]

Manuscript received March 6, 2013. This work was performed using HPC resources from GENCI-IDRIS (grant 2013-050779). The authors would like to thank the European Science Foundation (NEWFOCUS project), Brittany Region and CNRS (SAD project: BFN_SIW), ANR (VERSO/AMORCE project), DGA (ASTRID/GRAIK project) and FUI (DENOTEIC project).

G. Valerio, M. Casaletti, J. Seljan, M. Ettorre, and R. Sauleau are with the IETR (Institut d'Electronique et des Télécommunications de Rennes), UMR CNRS 6164, 35042 Rennes, France (e-mail: guido.valerio@univ-rennes1.fr).

M. Albani is with the Department of Information Engineering, University of Siena, Siena, Italy. (e-mail: matteo.albani@dii.unisi.it).

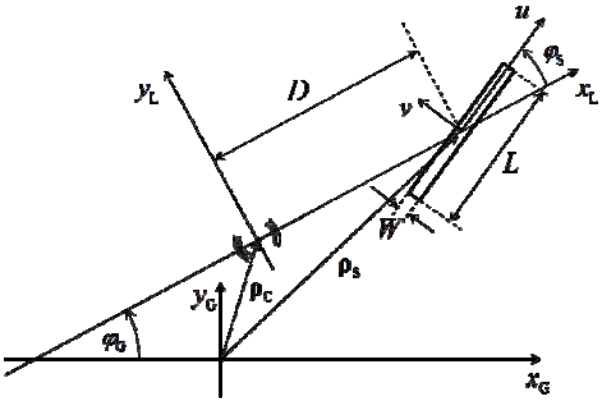

Fig. 1. Geometry of the problem analyzed in this paper.

$$\mathbf{M}_n\left(\boldsymbol{\rho},z;\kappa_\rho^{\mathrm{TM}}\right)=\nabla\times\left[\hat{\mathbf{z}}\psi_n^{\mathrm{TM}}\left(\boldsymbol{\rho},z;\kappa_\rho^{\mathrm{TM}}\right)\right],$$
$$\mathbf{N}_n\left(\boldsymbol{\rho},z;\kappa_\rho^{\mathrm{TM}}\right)=\frac{1}{k}\nabla\times\nabla\times\left[\hat{\mathbf{z}}\psi_n^{\mathrm{TE}}\left(\boldsymbol{\rho},z;\kappa_\rho^{\mathrm{TE}}\right)\right], \tag{3}$$

where k is the medium wavenumber. The scalar functions ψ are defined as follows

$$\psi_n^{\mathrm{TM}}\left(\boldsymbol{\rho},z;\kappa_\rho^{\mathrm{TM}}\right)=H_n^{(2)}\left(\kappa_\rho^{\mathrm{TM}}|\boldsymbol{\rho}|\right)e^{-jn\varphi}\chi^{\mathrm{TM}}\left(z;\kappa_\rho^{\mathrm{TM}}\right),$$
$$\psi_n^{\mathrm{TE}}\left(\boldsymbol{\rho},z;\kappa_\rho^{\mathrm{TE}}\right)=H_n^{(2)}\left(\kappa_\rho^{\mathrm{TE}}|\boldsymbol{\rho}|\right)e^{-jn\varphi}\chi^{\mathrm{TE}}\left(z;\kappa_\rho^{\mathrm{TE}}\right). \tag{4}$$

The functions χ depend on the stratification considered along z, and can be expressed in simple closed forms [16], [18].

The function **B** describes the equivalent magnetic current flowing on the aperture of a slot, which corresponds to a basis function in the MoM formulation. In the following, the formulation is kept general, so that different functions can be used. However, the numerical results shown in next section refer to the choice

$$\mathbf{B}\left(\boldsymbol{\rho}\right)=\hat{\mathbf{u}}B\left(u\right)=\hat{\mathbf{u}}\frac{1}{W}\sin\left[\frac{p\pi}{L}\left(u+\frac{L}{2}\right)\right] \tag{5}$$

for $-L/2 < u < L/2$, and $-W/2 < v < W/2$. The local Cartesian reference system (u,v) has its origin at the center of the slot, the u axis along its length L, and the v axis along its width W. The integer p describes the order of the function.

The integrals (1) and (2) can be computed in the spatial domain. This requires the computation of twofold integrals performed on the surface of a slot. In this section, we transform them into equivalent monodimensional spectral-domain integrals and investigate the most efficient numerical evaluation strategy.

Through a straightforward substitution of the Fourier transform of **M**, **N** and **B**, the integral can be expressed as the inverse Fourier transform

$$R_n^{\mathrm{TM}}\left(\boldsymbol{\rho}_{\mathrm{S}}-\boldsymbol{\rho}_{\mathrm{C}},z;\kappa_\rho^{\mathrm{TM}}\right)$$
$$=\frac{1}{\left(2\pi\right)^2}\int_{-\infty}^{+\infty}\int_{-\infty}^{+\infty}\tilde{\mathbf{B}}\left(-\mathbf{k}_\rho\right)\cdot\tilde{\mathbf{M}}_n\left(k_x,k_y,z;\kappa_\rho^{\mathrm{TM}}\right)e^{-jk_xD}\mathrm{d}k_x\mathrm{d}k_y \tag{6}$$

$$R_n^{\mathrm{TE}}\left(\boldsymbol{\rho}_{\mathrm{S}}-\boldsymbol{\rho}_{\mathrm{C}},z;\kappa_\rho^{\mathrm{TE}}\right)$$
$$=\frac{1}{\left(2\pi\right)^2}\int_{-\infty}^{+\infty}\int_{-\infty}^{+\infty}\tilde{\mathbf{B}}\left(-\mathbf{k}_\rho\right)\cdot\tilde{\mathbf{N}}_n\left(k_x,k_y,z;\kappa_\rho^{\mathrm{TE}}\right)e^{-jk_xD}\mathrm{d}k_x\mathrm{d}k_y \tag{7}$$

Here a local Cartesian coordinate system $\left(x_{\mathrm{L}},y_{\mathrm{L}}\right)$ has been used, whose origin is placed in $\boldsymbol{\rho}_{\mathrm{C}}$ and whose x axis is chosen along the source-slot direction, where $\mathbf{k}_\rho=k_x\hat{\mathbf{x}}_{\mathrm{L}}+k_y\hat{\mathbf{y}}_{\mathrm{L}}$. D is the distance between the center of the slot and the source (Fig. 1).

The Fourier transform of **B** is

$$\tilde{\mathbf{B}}\left(\mathbf{k}_\rho\right)=\hat{\mathbf{u}}\tilde{B}\left(k_u,k_v\right)$$
$$=\hat{\mathbf{u}}2j^{n+1}\frac{n\pi}{L}\frac{\sin\left[\frac{L}{2}\left(k_u+\frac{p\pi}{L}\right)\right]}{k_u^2-\left(\frac{p\pi}{L}\right)^2}\frac{\sin\left(\frac{Wk_v}{2}\right)}{\frac{Wk_v}{2}} \tag{8}$$

with the transverse spectral vector $\mathbf{k}_\rho=k_u\hat{\mathbf{u}}+k_v\hat{\mathbf{v}}$ expressed in the (u,v) slot reference system.

The u-components of the transforms of **M** and **N** are (see the Appendix for some details)

$$\begin{Bmatrix}\hat{\mathbf{u}}\cdot\tilde{\mathbf{M}}_n\left(k_x,k_y,z\right)\\ \hat{\mathbf{u}}\cdot\tilde{\mathbf{N}}_n\left(k_x,k_y,z\right)\end{Bmatrix}=4j^ne^{-jn\varphi_{\mathrm{G}}}\begin{Bmatrix}\mathbf{k}_\rho\cdot\hat{\mathbf{v}}\chi^{\mathrm{TM}}\left(z;\kappa_\rho^{\mathrm{TM}}\right)\\ \frac{\mathbf{k}_\rho\cdot\hat{\mathbf{u}}}{k}\frac{\mathrm{d}}{\mathrm{d}z}\chi^{\mathrm{TE}}\left(z;\kappa_\rho^{\mathrm{TE}}\right)\end{Bmatrix}$$
$$\times\frac{\left[k_x-j\,\mathrm{sgn}\left(n\right)k_y\right]^{|n|}}{\left(\kappa_\rho^{\mathrm{TM/TE}}\right)^{|n|}}\frac{1}{k_x^2+k_y^2-\left(\kappa_\rho^{\mathrm{TM/TE}}\right)^2}, \tag{9}$$

where φ_{G} is the angle between the local x axis and the global x axis (see Fig. 1). The two integrals (6) and (7) become

$$\begin{Bmatrix}R_n^{\mathrm{TM}}\left(\boldsymbol{\rho}_{\mathrm{S}},z'\right)\\ R_n^{\mathrm{TE}}\left(\boldsymbol{\rho}_{\mathrm{S}},z'\right)\end{Bmatrix}=\frac{j^ne^{jn\varphi_{\mathrm{G}}}}{\pi^2}\begin{Bmatrix}\chi^{\mathrm{TM}}\left(z;\kappa_\rho^{\mathrm{TM}}\right)I_n^{\mathrm{TM}}\left(\kappa_\rho^{\mathrm{TM}},D\right)\\ \frac{1}{k}\frac{\mathrm{d}}{\mathrm{d}z}\chi^{\mathrm{TE}}\left(z;\kappa_\rho^{\mathrm{TE}}\right)I_n^{\mathrm{TE}}\left(\kappa_\rho^{\mathrm{TE}},D\right)\end{Bmatrix} \tag{10}$$

where

$$I_n^{\mathrm{TM/TE}}\left(\kappa_\rho^{\mathrm{TM/TE}},D\right)=\int_{-\infty}^{+\infty}\int_{-\infty}^{+\infty}\tilde{f}^{\,\mathrm{TM/TE}}\left(k_x,k_y\right)$$
$$\times\frac{\left[k_x-j\,\mathrm{sgn}\left(n\right)k_y\right]^{|n|}}{\left(\kappa_\rho^{\mathrm{TM/TE}}\right)^{|n|}}\frac{e^{-jk_xD}}{k_x^2+k_y^2-\left(\kappa_\rho^{\mathrm{TM/TE}}\right)^2}\mathrm{d}k_x\mathrm{d}k_y, \tag{11}$$

$$\tilde{f}^{\,\mathrm{TM}}\left(k_x,k_y\right)=\mathbf{k}_\rho\cdot\hat{\mathbf{v}}\tilde{B}\left(-\mathbf{k}_\rho\cdot\hat{\mathbf{u}},-\mathbf{k}_\rho\cdot\hat{\mathbf{v}}\right) \tag{12}$$

and

$$\tilde{f}^{\,\mathrm{TE}}\left(k_x,k_y\right)=\mathbf{k}_\rho\cdot\hat{\mathbf{u}}\tilde{B}\left(-\mathbf{k}_\rho\cdot\hat{\mathbf{u}},-\mathbf{k}_\rho\cdot\hat{\mathbf{v}}\right) \tag{13}$$

The k_x integration in (11) should be performed in the complex k_x plane along the Sommerfeld path in Fig. 2: it consists in a suitable deformation of the real axis in order to avoid the possible singularity on the real axis. As $k_{x_{\mathrm{I}}}=\Im\mathrm{m}\left\{k_x\right\}\to-\infty$, the kernel of the integrand decays exponentially as $e^{k_{x_{\mathrm{I}}}D}$. On the other hand, the functions $\tilde{f}$

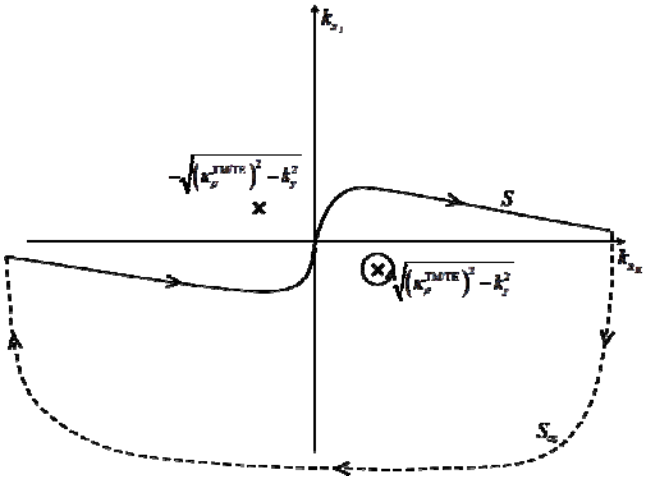

Fig. 2. Complex k_x plane where the integrand in (11) is defined. The residues at $k_x = \sqrt{\left(\kappa_\rho^{\mathrm{TM/TE}}\right)^2 - k_y^2}$ are shown. The integration along the Sommerfeld path (*solid line*) is equivalent to the residue in the lower half plane (encircled), since the half circle at infinity (*dashed line*) gives no contribution to the integration if $D > \max(L,W)/2$.

increase exponentially as $\exp\left[-k_{x_j}\hat{\mathbf{x}}_{\mathrm{L}}\cdot\left(L\hat{\mathbf{u}}+W\hat{\mathbf{v}}\right)/2\right]$; this follows from the exponential behavior $\sin(jx)\cong e^x/2$ of the sin functions of imaginary arguments in (8) and from the relation among k_u, k_v and k_x (algebraic terms are neglected in all these asymptotic evaluations). Provided that $D > \hat{\mathbf{x}}_{\mathrm{L}}\cdot\left(L\hat{\mathbf{u}}+W\hat{\mathbf{v}}\right)/2$, the exponential decay of the integrand kernel is faster than the exponential rise of $\tilde{f}$, and the overall integrand is infinitesimal as $\Im\mathrm{m}\{k_x\}\to-\infty$. If $W \cong L$, this convergence conditions is certainly fulfilled if $D > L/2$. Note that different choices of the current in (5) could lead to different lower limits for the distance D. However, the method here proposed will always hold in the correct convergence region for D. The exponential decay of the integrand on the semicircle at infinity grants the equivalence between the Sommerfeld integration and the integration along the closed path formed by the Sommerfeld path and the semicircle. The k_x integral is then equal to the sum of the residues of the singularities enclosed by this closed path. In our case, the only singularity is the pole present in the lower plane at $k_x = \sqrt{\left(\kappa_\rho^{\mathrm{TM/TE}}\right)^2 - k_y^2}$. The integrals (11) are then transformed in one-dimensional k_y-integrals

$$I_{n,m}^{\mathrm{TM/TE}}(D) = -2\pi j\int_{-\infty}^{+\infty}\tilde{f}^{\mathrm{TM/TE}}\left(k_x,k_y\right) \times\frac{\left[k_x - j\,\mathrm{sgn}(n)k_y\right]^{|n|}}{\left(\kappa_\rho^{\mathrm{TM/TE}}\right)^{|n|}}\frac{e^{-j\sqrt{\left(\kappa_\rho^{\mathrm{TM/TE}}\right)^2-k_y^2}D}}{2\sqrt{\left(\kappa_\rho^{\mathrm{TM/TE}}\right)^2-k_y^2}}\mathrm{d}k_y \quad (14)$$

The integration in (14) is performed along a Sommerfeld integration path of the same shape as the one shown in Fig. 2, avoiding the pair of branch points at $k_y = \pm\kappa_\rho$. Such an integration path lies on the Riemann sheet defined by $\Im\mathrm{m}\sqrt{\kappa_\rho^2 - k_y^2} \le 0$, in order to grant convergence for large D. A suitable change of variable can transform the integrand and the Sommerfeld integration path into a new function having Gaussian decay along the new integration path. This new path would correspond to the SDP of the integrand in (14); it would be particularly attractive since it allows for an easy numerical evaluation of (14), with a reduced number of quadrature points. The SDP is the path passing through the so called "saddle point" (SP) of the integrand. The SP is the point in the k_y complex plane where the phase gradient of the integrand is zero (i.e., the stationary point of the phase). Once the SP location is determined, the SDP crosses the SP with a slope aligned along the direction of constant phase and maximum decay of the integrand.

If an asymptotic evaluation for large D of the integral were attempted, both the integrand value and the SDP slope at the SP would be required. Specifically, the SP would be located by finding the stationary point of the phase of the exponential factor in (14), the term providing the dominant phase variation for large D.

However, our aim is here the exact computation of the integral for moderate D. In this connection, we define the SP point as the stationary point of the phase of the complete kernel in (14). Only the phase variation of $\tilde{f}$ is neglected, since the slot dimensions are assumed to be small if compared to the distance D. In this case, the phase of the current $\tilde{\mathbf{B}}$ will be almost constant over a wide spectral region. As a consequence of this hypothesis, the obtained results will be independent on the choice of **B**.

Furthermore, the result and the performance of the numerical integration will be unchanged even if the path is slightly moved from the exact SDP, provided no singularities are crossed and the Gaussian decay is met on the integrand tail. For this reason, the exact direction of the SDP at the SP will not be investigated in the following subsections.

As said, the requested path is obtained by performing suitable change of variables, depending on the value of the radial wavenumber κ_ρ. The two cases of real value (propagating radial mode) and imaginary value (evanescent radial mode) are analyzed separately in the following.

A. Propagating radial mode

With the substitution $k_y = \kappa_\rho s\sqrt{2j+s^2}$, implicitly defining the complex variable s, it follows that $k_x = \kappa_\rho\left(1-js^2\right)$ and

$$I_n^{\mathrm{TM/TE}} = -\pi j\sqrt{2j}e^{-j\kappa_\rho D}\int_{-\infty}^{+\infty}\tilde{f}^{\mathrm{TM/TE}}\left(k_x,k_y\right)\tilde{K}_n(s)\mathrm{d}s, \quad (15)$$

where the kernel $\tilde{K}_n$ is

$$\tilde{K}_n(s) = \left[1+j\left(s^2-\mathrm{sgn}(n)s\sqrt{2j+s^2}\right)\right]^{|n|}\frac{e^{-\kappa_\rho Ds^2}}{\sqrt{1-js^2/2}}\mathrm{d}s. \quad (16)$$

The k_y Sommerfeld integration path in (14) is mapped into the real s axis in (15), provided that $\Im\mathrm{m}\sqrt{2j+s^2} \ge 0$ in the

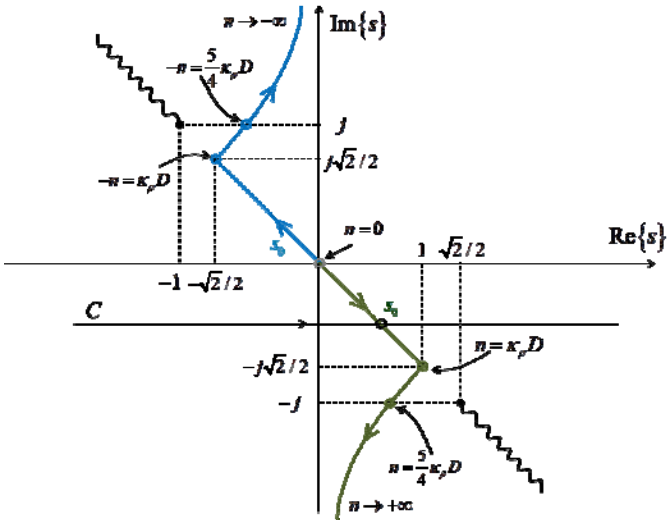

Fig. 3. Complex s plane where the integrand in (15) is defined. The trajectories of the point s_0 are shown for positive and negative n in green and blue, respectively, as the magnitude of the index n increases. The integration path C is shown for a given s_0 in the case $n > 0$.

definition of k_y. The condition $\Im\mathrm{m}\sqrt{\kappa_\rho^2 - k_y^2} \le 0$ must not be enforced problems since k_x is not defined through any square root. This is due to the fact that the change of variable has removed the branch point present in (14).

However, in this transformed complex s plane, a new pair of branch points is present at $s_\mathrm{b}^\pm = \pm\sqrt{2j}$, due to the square root in the denominator. This square root arises from a k_y term in the differential $\mathrm{d}k_y$ in (14), and its determination should then be chosen accordingly. From the definition of k_y, $\Im\mathrm{m}\sqrt{2j + s^2} \ge 0$, and consequently $\Re\mathrm{e}\sqrt{1 - js^2/2} \ge 0$. This condition leads to define branch cuts along the lines $s_\mathrm{R} = -s_\mathrm{J}$, $s_\mathrm{R} s_\mathrm{J} < -1$ (where $s = s_\mathrm{R} + j\, s_\mathrm{J}$), i.e., along the bisecting line of the second and fourth quadrant (the cuts are shown in Fig. 3 in wavy lines). Any deformation of the real-axis integration path cannot cross these lines.

The SP s_0 of the kernel $\tilde{K}$ can be easily determined: the kernel is expressed in the exponential form $\exp[\psi(s)]$, through a suitable function $\psi(s)$:

$$\psi(s) = -\kappa_\rho D s^2 + |n| \ln\left\{1 + j\left[s^2 - \mathrm{sign}(n) s\sqrt{2j + s^2}\right]\right\} - \frac{1}{2}\ln\left(1 - j\frac{s^2}{2}\right) \quad (17)$$

If $4\kappa_\rho D \gg 1$, the point s_0 can be found in closed form as a solution of the equation $\mathrm{d}\psi/\mathrm{d}s = 0$:

$$s_0 = \mathrm{sgn}(n)\, e^{-j\frac{\pi}{4}} \sqrt{1 - \sqrt{1 - \left(\frac{n}{\kappa_\rho D}\right)^2}}\,, \quad (18)$$

The integral (15) can then be evaluated with the simple substitution $s \to s + s_0$, and the integration can be kept along the horizontal line with constant imaginary parts C, granting a Gaussian convergence. Indeed, the correct SDP should cross the point s_0 with a certain slope possibly depending on n. However, according to the previous comments we will be content to use a path C which crosses the SP s_0 and grants a Gaussian convergence on the integrand tail. Such a path will be referenced here as the SDP of the integral. In Fig. 3 the SDP C is named C_+ or C_- according to the sign of n.

Of course, the SP s_0 moves on the complex s plane as the value of $|n|/\kappa_\rho D$ changes. The curve described by s_0 is shown in Fig. 3: the two branches in green and blue refer to the cases $n > 0$ and $n < 0$, respectively. The arrows refer to the directions of the SP as $|n|$ increases. If $|n| < \kappa_\rho D$, the SP moves on the bisecting line of the second and fourth quadrant, and the horizontal integration path does not crosses the branch cut. However, as $|n|$ increases, eventually $\mathrm{Im}(s_0) = \mathrm{Im}(s_\mathrm{b}^\pm)$, when $|n| = 5\kappa_\rho D/4$. For higher values of $|n|$, the horizontal integration path cannot be chosen, since it would cross one of the branch cuts. An SDP path could still be rigorously obtained by a suitable deformation around the branch cut. However, such a problem is not addressed here, since the corresponding range of values of $|n|/(\kappa_\rho D) > 5/4$ is beyond the limit of usual applications of interest.

It should be highlighted that the trajectories described in Fig. 3 as $|n|$ increases, can be alternatively regarded as the trajectories of the SP as the electrical distance $\kappa_\rho D$ between the vertical source and the slot decreases.

B. Evanescent radial mode

A similar approach can be adopted for the evaluation of the integral (14) when κ_ρ is imaginary: the cylindrical mode considered decays exponentially along radial directions.

The change of variable required is $k_y = j\kappa_\rho s\sqrt{2 + s^2}$. It follows that $k_x = \kappa_\rho(1 + s^2)$ and

$$I_n^{\mathrm{TM/TE}} = -\sqrt{2}\pi e^{-j\kappa_\rho D} \int_{-\infty}^{+\infty} \tilde{f}^{\mathrm{TM/TE}}(k_x, k_y)\, \tilde{K}_n(s)\, \mathrm{d}s\,, \quad (19)$$

with

$$\tilde{K}_n(s) = \left(1 + s^2 - \mathrm{sign}(n) s\sqrt{2 + s^2}\right)^{|n|} \frac{e^{-\kappa_\rho D s^2}}{\sqrt{1 + s^2/2}}\,\mathrm{d}s\,. \quad (20)$$

The Sommerfeld k_y integration path in (14) (equivalent to the real axis in this case) becomes the real axis on the s complex plane, provided that $\Im\mathrm{m}\sqrt{2 + s^2} \ge 0$ in the definition of k_y. As in the previous subsection, the branch cuts in (14) vanish due to the change of variable.

However, a new pair of branch points is present at $s_\mathrm{b}^\pm = \pm j\sqrt{2}$, due to the square root in the denominator. Since these square roots originate from the differential $\mathrm{d}k_y$ in (14), its determination should be chosen accordingly. From the expression of k_y, $\Im\mathrm{m}\sqrt{2 + s^2} \ge 0$ is required. This condition

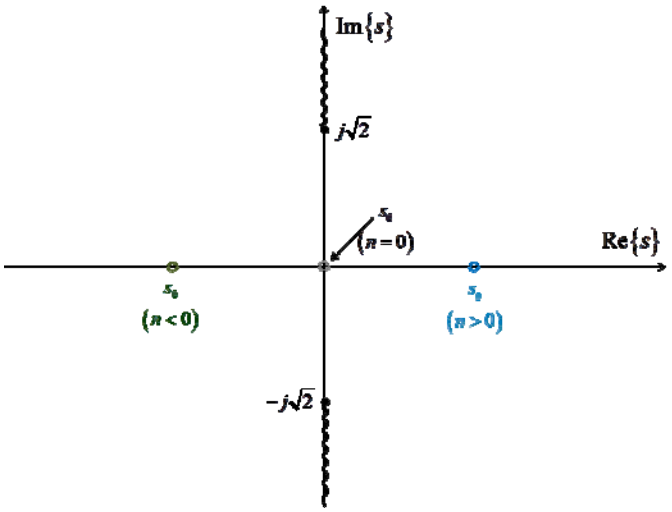

Fig. 4. Complex s plane where the integrand in (19) is defined. The point s_0 is shown for positive and negative n values, in blue and green, respectively The point $s_0 = 0$, corresponding to the case $n = 0$, is also shown.

leads to define branch cuts along the lines $s_R = 0$, $s_J > \sqrt{2}$ (where $s = s_R + js_J$), i.e., along the imaginary axis (the cuts are shown in Fig. 4 in wavy lines). Any deformation of the real-axis integration path cannot cross these lines.

The SP s_0 of the kernel $\tilde{K}$ can be easily determined as done in the previous subsection. The kernel is expressed in the exponential form $\exp[\psi(s)]$, through a suitable function $\psi(s)$:

$$\psi(s) = -\kappa_\rho D s^2 + |n| \ln\left[1 + s^2 - \mathrm{sign}(n) s\sqrt{2+s^2}\right] - \frac{1}{2}\ln\left(1+\frac{s^2}{2}\right) \quad (21)$$

Again in the hypothesis $4|\kappa_\rho| D \gg 1$, we obtain from the equation $d\psi/ds=0$:

$$s_0 = \mathrm{sign}(n)\sqrt{-1+\sqrt{1+\left(\frac{n}{|\kappa_\rho| D}\right)^2}} \quad (22)$$

lying on the real axis for every azimuthal mode and for any electrical distance between the slot and the vertical post. The integration path is chosen in this case as the real axis itself, around the point s_0, by performing the simple change of variable $s \to s + s_0$. No issues are encountered in this case due to the crossing of the branch cut, and no limit of validity exists.

Further manipulation of both integrals (15) and (19) could yield suitable asymptotic evaluations and so avoid any numerical integration. However, this study is not addressed here in order to keep the final results independent on the choice of the current **B**. In fact, an asymptotic evaluation will require the computation of first- and second-order derivatives of the integrand, which can be expressed in closed forms once the functional dependence of **B** is determined. Indeed, these derivatives could also be performed through numerical differentiation. Unfortunately, this strategy would require the computation of a certain number of samples of $\tilde{\mathbf{B}}$ in order to implement finite differences. The computational effort would then be moved from the computation of integrand samples for the direct integration on the SDP, to the computation of samples of $\tilde{\mathbf{B}}$ for the numerical differences needed for the asymptotic evaluation.

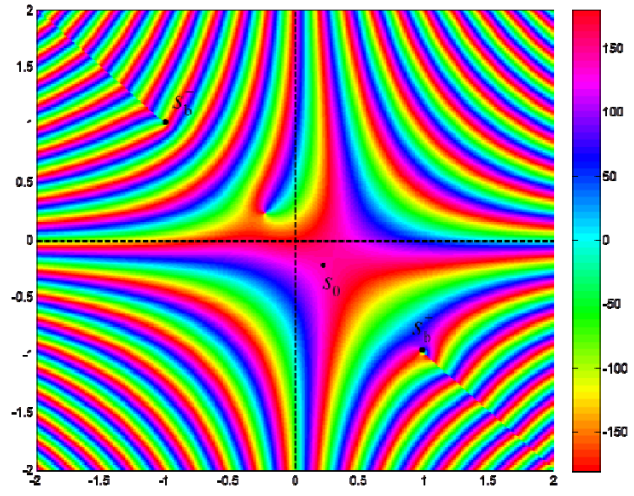

(a)

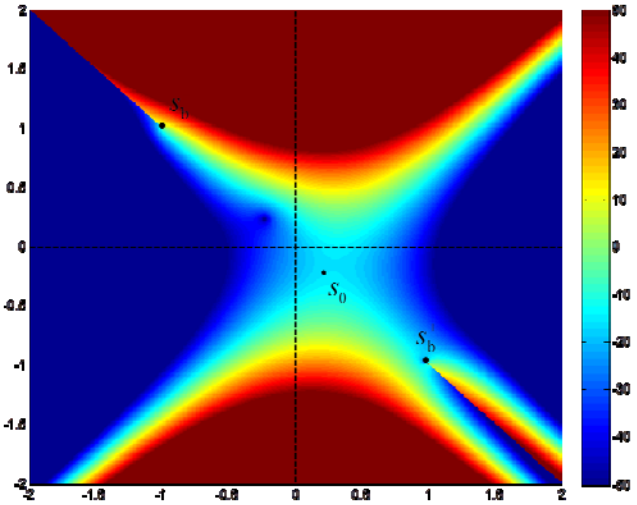

(b)

Fig. 5. Integrand of (15) in the complex s plane. Geometric and physical parameters: f = 5 GHz, $\kappa_\rho D = \pi$, n = 3, W = 0.5 mm, L = 3 mm. (a) phase in degrees, (b) magnitude in dB.

III. Numerical Results

Numerical results are discussed here in order to validate the theoretical analysis presented in the previous section.

The phase and magnitude of the integrand of $I^{TM/TE}$ for typical values of geometrical parameters is shown in Fig. 5 for a propagating radial mode, and in Fig. 6 for an evanescent radial mode. The SP s_0 is also highlighted. A constant-phase path is well approximated on a curve with constant imaginary part (horizontal line). Such a curve will be used for the numerical evaluation of the integral. The Gaussian decay is also evident in the magnitude plot along the horizontal

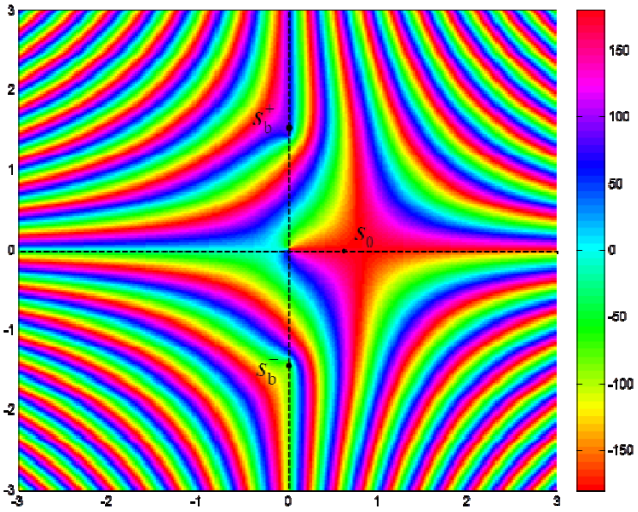

(a)

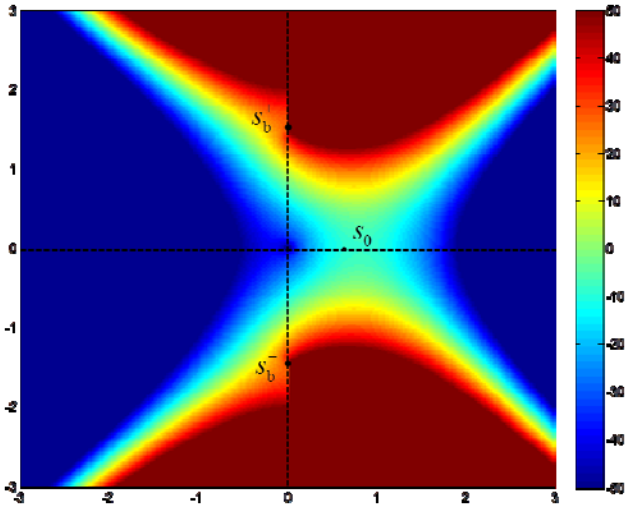

(b)

Fig. 6. Integrand of (19) in the complex s plane. Geometric and physical parameters: f = 5 GHz, $\kappa_\rho D = -j3$, n = 3, W = 0.5 mm, L = 3 mm. (a) phase in degrees, (b) magnitude in dB.

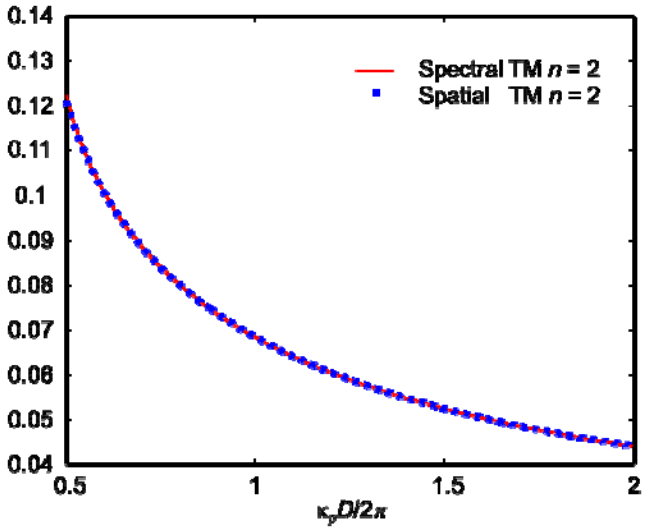

(a)

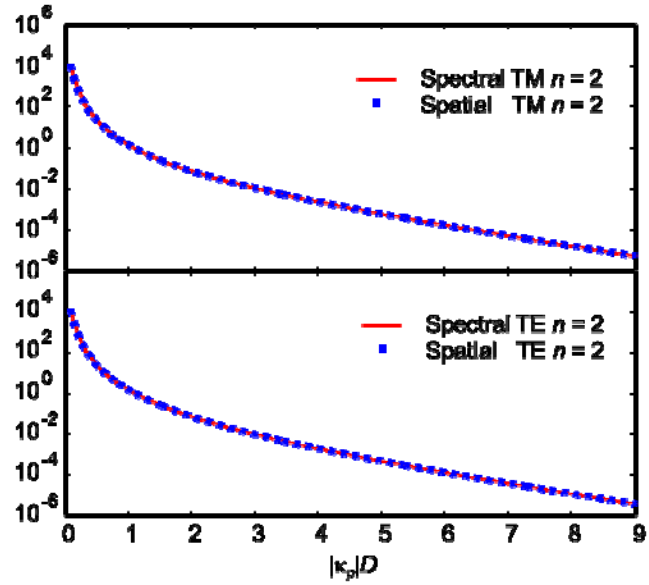

(b)

Fig. 7. Integral (19) computed with the spatial and the spectral integration, for different values of the mutual distance D between the slot and the line source. Geometric and physical parameters: f = 5 GHz, n = 3, W = 0.5 mm, L = 3 mm, $\varphi_L = \pi/3$ (a) TM propagating mode, (b) TM and TE evanescent modes.

direction, while a Gaussian amplification is shown along the vertical axis as expected.

The integrals have been computed through the spectral forms (15), (19), and their spatial counterparts (1), (2). The spectral integrals are computed through Gaussian-Hermite integration scheme, in order to take advantage of the Gaussian decay of the integrand. The spatial integrals are computed through a Gaussian integration scheme [19].

The results are compared in Fig. 7 for different distances between the slot and the vertical post. For propagating modes, distances D are restricted in the interval $D > \max\left\{4|n|/\left(5\kappa_\rho\right), L/2\right\}$, in order to prevent the crossing between the integration path and a branch cut, and to grant the validity of (14). This condition covers most of the cases of practical interest even for moderate values of $|n|$. For evanescent modes, the range of distances $D > L/2$ is chosen. The perfect agreement between the two computation methods confirms the validity of the proposed approach.

A study on the quadrature points required for the two integration methods has been performed. Its results are summarized in Fig. 8, where the relative error is shown for two typical cases of small and average-sized slot, with reference to a propagating TM radial mode. The error is computed by assuming as an exact result the spectral expression integrated with 300 points. A very small number of points is always sufficient to obtain a satisfactory accuracy with the spectral approach for a very wide of geometrical parameters. Of course, convergence improves as the mutual normalized distance $\kappa_\rho D$ increases, and as the size of the slot decreases.

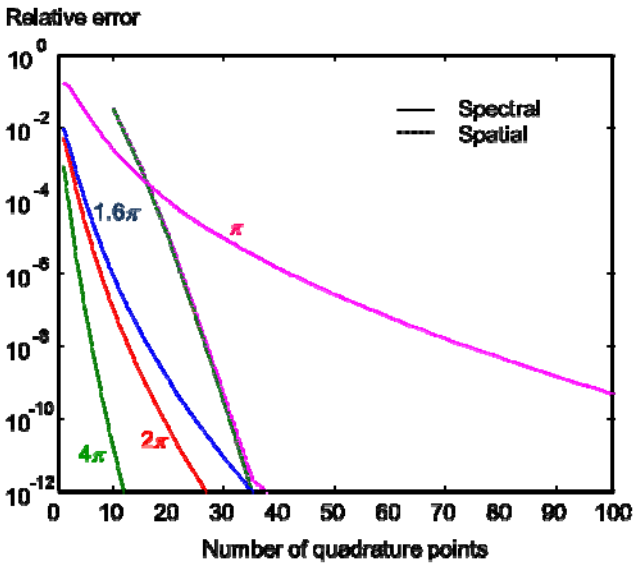

(a)

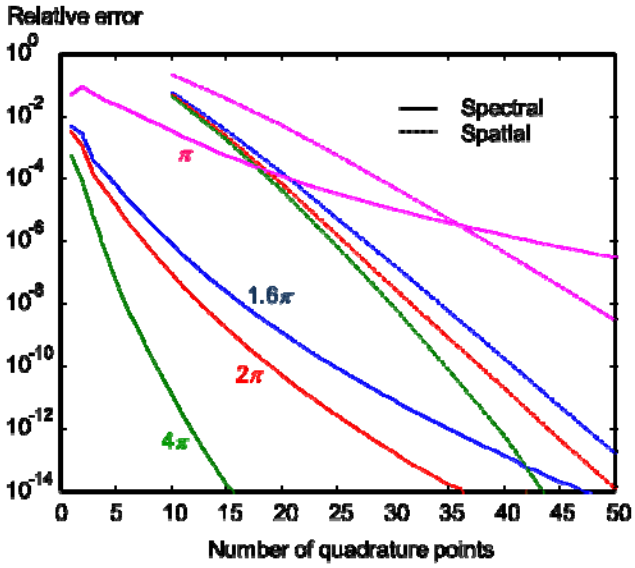

(b)

Fig. 8. Relative error vs. number of quadrature points used to compute the spectral integral (15) (*solid lines*) and the spatial integral (1) (*dashed lines*) for a TM propagating mode. A propagating radial mode is considered. Different distances are examined as explained in the pictures: $\kappa_\rho D = 4\pi$ (*green line*), $\kappa_\rho D = 2\pi$ (*red line*), $\kappa_\rho D = 1.6\pi$ (*blue line*), $\kappa_\rho D = \pi$ (*pink line*). Geometric and physical parameters: f = 5 GHz, n = 3, $\varphi_L = \pi/3$. (a) Small slot: W = 0.5 mm, L = 3 mm. (b) Large slot: W = 2 mm, L = 30 mm.

This is due to the fact that for large $\kappa_\rho D$ the spectral integral is better approximated by the integrand behavior in the neighborhood of the SP while the tails become less significant. In this limit, the integral is approaching to its asymptotic estimation, depending on the local behavior of the integrand in the SP. On the other hand, as the slot size is reduced, the spectrum of the current **B** is more uniform and does not perturb the SP location, here determined neglecting the phase of $\tilde{\mathbf{B}}$ [see the discussion after (14)].

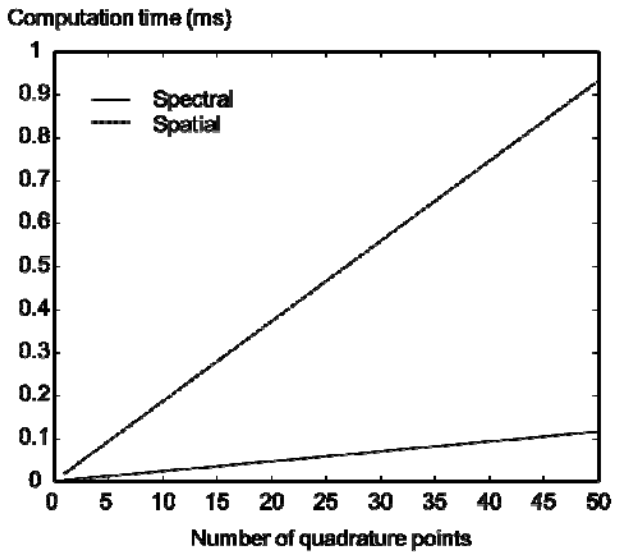

Fig. 9. Computation time to numerically integrate the spectral integral (solid line) and the spatial integral (dashed line) when varying the number of quadrature points used. Geometric and physical parameters as in Fig. 8(b), and $\kappa_\rho D = \pi$.

As expected, the number of quadrature points of the spatial integral depends on the size of the slot considered, while they are quite independent on the normalized distance $\kappa_\rho D$. This is due to the fact that the accuracy of the spatial integration depends on the spatial smoothness of the integrand: provided the slot is sufficiently far from the origin of the cylindrical wave in order to avoid near-singular fields, the field variability is mainly dictated by the slot size.

For reasonable accuracies, the number of spatial points is always considerably larger than the number of spectral points, unless the slot size is extremely small and the distance D is smaller than half a wavelength [pink curve in Fig. 8(a)].

The computation of the kernel in the spatial integrand involves various special functions (Hankel functions and complex exponentials), while the computation of the kernel in the spectral integrand only requires algebraic operations. For this reason a comparison is necessary between the computation time of the two integrals, once the number of quadrature points is chosen. The relevant results are shown in Fig. 9, where the computation time in ms is measured on a Xeon E5540 2.83 GHZ with 64 GB RAM. As expected, a remarkable improvement is obtained when computing the spectral integral. This improvement holds even when the number of points required is multiplied by a factor five with respect to the spatial integration, a limiting case never encountered in practical problems as shown in Figs. 8. Combining the results in Figs. 8 and 9, an average speed-up factor of 30 is obtained through the novel spectral formulation in most cases of interest.

The spectral computation has been implemented in a full-wave code modeling SIW slot antennas [17]. As a final example, the speed-up factor and the accuracy obtained in the analysis of a complete structure is here presented. The

structure consists of 23 rectangular waveguides whose side walls are realized through a series of vertical metallic posts. All the waveguides are fed in phase with a coaxial cable, and a matching metallic post is placed close to each cable for matching purposes. Radiation is achieved through slots etched in the top wall (see Fig. 10). A total number of 2223 metallic posts and 184 slots are present (8 per waveguide). Three azimuthal modes are retained on each post (n = 0, ±1), and only the m = 0 parallel-plate-waveguide vertical mode is considered, with $\kappa_\rho = k$. In Fig. 11, the normalized radiation patterns at 24.4 GHz are compared on the two principal planes. The results obtained with the spectral and with the spatial computation of the post-slot coupling are perfectly superimposed, thus validating once more the accuracy of the approach. In Table I, the total computation time of the analysis is shown with the spatial and the spectral integrals. This leads to a total speed-up factor of 2, obtained as the ratio between the spatial and spectral computation times. Specifically, also the computation time required to compute only the coupling integrals is also shown, where a sped-up factor of 25 is obtained. This confirms the results previously discussed in this section.

TABLE I
CPU SIMULATION TIME ON A XEON E5540 2.83GHZ WITH 64 GBYTE RAM

	Spatial integration	Spectral integration	Speed-up factor
Integral computation	504.36 s	19.78 s	25.5
Complete simulation	901.89 s	416.53 s	2.17

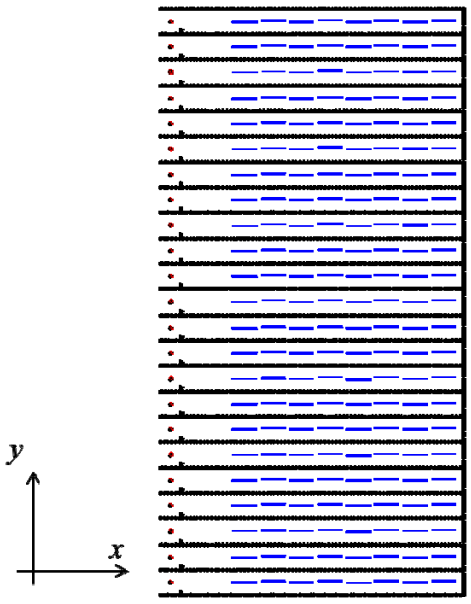

Fig. 10. Top view of the SIW structure considered for the full-wave analysis. Physical and geometrical parameters: thickness of the substrate h = 0.508 mm, dielectric constant ε_r =2.2. Each waveguide is 66.4 mm long and 5.6 mm wide. The slots are in shown in blue. The radius of each post is 0.2 mm.

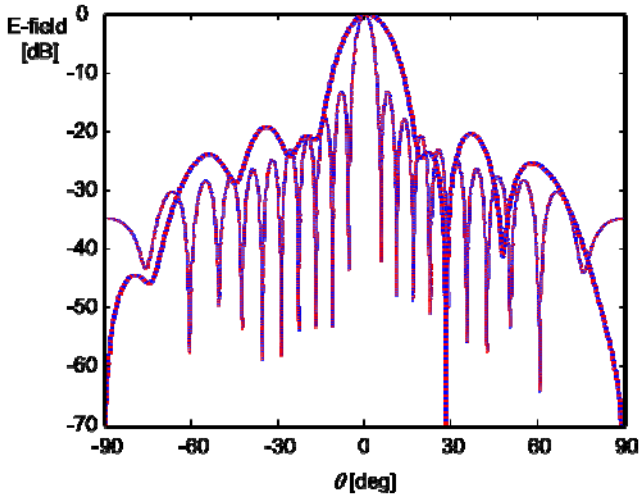

Fig. 11. Normalized radiation patterns of the structure in Fig. 10 vs. elevation angle θ at 24.15 GHz. All the coaxial feeds are simultaneously excited in phase. Computation of spatial integrals (*red lines*), computation of spectral integrals (*blue lines*). Principal planes φ = 0° (*thick lines*) and φ = 90° (*thin lines*).

IV. CONCLUSION

We have proposed a novel approach for the computation of the coupling between a cylindrical wave with arbitrary azimuthal dependence, and a slot placed on a plane orthogonal to the exciting line source. The spatial integral defining the coupling is replaced by an equivalent spectral integral performed along a SDP-like path in a transformed complex domain. A rigorous motivation of the approach has been described, together with the limit of validity of the final theoretical results. Numerical results have been shown to confirm the analysis and to investigate the convergence feature of the novel spectral integral. The proposed approach has been implemented in a hybrid MoM-MM code optimized for SIW antennas, in order to shown the acceleration obtained with respect to the simple spatial integration.

APPENDIX

The Fourier transforms of the cylindrical vector functions (3) are here rigorously computed. We start from the Fourier transform of the cylindrical scalar functions (4). As concerns the scalar functions, the two polarization only differ for their z-dependence. Since the transform is performed on a plane orthogonal to z, only one transformation is required. The transformation is performed in the local reference system (x_L,y_L), $\boldsymbol{\rho}_L = \boldsymbol{\rho} - \boldsymbol{\rho}_C = \rho_L \cos\varphi_L \hat{\mathbf{x}}_L + \rho_L \sin\varphi_L \hat{\mathbf{y}}_L = x_L \hat{\mathbf{x}}_L + y_L \hat{\mathbf{y}}_L$. The radial dependence of ψ is easily expressed in the local system, since the local radial coordinate is $\rho_L = |\boldsymbol{\rho} - \boldsymbol{\rho}_C|$. The global azimuth angle φ can be expressed in the local system as $\varphi_L = \varphi - \varphi_G$. We have

$$\tilde{\psi}_n(\mathbf{k}_\rho, z; \kappa_\rho) = \chi(z; \kappa_\rho) e^{-jn\varphi_G} \times \int_{-\infty}^{+\infty}\int_{-\infty}^{+\infty} H_n^{(2)}(\kappa_\rho \rho_L) e^{-jn\varphi_L} e^{-j(k_x x_L + k_y y_L)} dx_L dy_L \quad (23)$$

The above integral can be performed in cylindrical coordinates as

$$\begin{aligned}&\int_0^{+\infty} H_n^{(2)}\left(\kappa_\rho\rho_{\mathrm{L}}\right)\int_0^{2\pi} e^{-jn\varphi_{\mathrm{L}}}e^{-jk_\rho\rho_{\mathrm{L}}\cos(\varphi_{\mathrm{L}}-\alpha)}\rho_{\mathrm{L}}\mathrm{d}\rho_{\mathrm{L}}\mathrm{d}\varphi_{\mathrm{L}}\\&=\int_0^{+\infty} H_n^{(2)}\left(\kappa_\rho\rho_{\mathrm{L}}\right)\left[2\pi(-j)^n e^{-jn\alpha}J_{-n}\left(k_\rho\rho_{\mathrm{L}}\right)\right]\rho_{\mathrm{L}}\mathrm{d}\rho_{\mathrm{L}}\\&=2\pi j^n e^{-jn\alpha}\int_0^{+\infty} H_n^{(2)}\left(\kappa_\rho\rho_{\mathrm{L}}\right)J_n\left(k_\rho\rho_{\mathrm{L}}\right)\rho_{\mathrm{L}}\mathrm{d}\rho_{\mathrm{L}}\end{aligned}\quad(24)$$

where $\rho_{\mathrm{L}}=\sqrt{x_{\mathrm{L}}^2+y_{\mathrm{L}}^2}$, $k_x=k_\rho\cos\alpha$, and $k_y=k_\rho\sin\alpha$. The ρ_{L}-integral can be solved through the closed formula in [19], valid for $n>0$. The final result is

$$\begin{aligned}&\tilde{\psi}_n\left(k_x,k_y,z;\kappa_\rho\right)=\\&=\chi\left(z;\kappa_\rho\right)e^{-jn\varphi_{\mathrm{G}}}2\pi j^n e^{-jn\alpha}\frac{2j}{\pi}\frac{k_\rho^{|n|}}{\kappa_\rho^{|n|}\left(k_\rho^2-\kappa_\rho^2\right)}\\&=4j^{n+1}e^{-jn\varphi_{\mathrm{G}}}\chi\left(\kappa_\rho,z\right)\frac{\left[k_x-j\,\mathrm{sgn}(n)k_y\right]^{|n|}}{\kappa_\rho^{|n|}}\frac{1}{k_x^2+k_y^2-\kappa_\rho^2}\end{aligned}\quad(25)$$

since $k_\rho^{|n|}e^{-jn\alpha}=\left[k_x-j\,\mathrm{sgn}(n)k_y\right]^{|n|}$.

The component of the transform of the vector wave functions along the direction $\hat{\mathbf{u}}$ can be easily obtained from the spectral form of the ∇ operator; i.e., $\nabla=-j\mathbf{k}_\rho+\hat{\mathbf{z}}\frac{\partial}{\partial z}$, thus obtaining

$$\begin{aligned}&\hat{\mathbf{u}}\cdot\tilde{\mathbf{M}}_n\left(k_x,k_y,z\right)=4j^n e^{-jn\varphi_{\mathrm{G}}}\chi\left(z;\kappa_\rho\right)\left(\hat{\mathbf{u}}\cdot\mathbf{k}_\rho\times\hat{\mathbf{z}}\right)\\&\times\frac{\left[k_x-j\,\mathrm{sgn}(n)k_y\right]^{|n|}}{\kappa_\rho^{|n|}}\frac{1}{k_x^2+k_y^2-\kappa_\rho^2}\end{aligned}\quad(26)$$

and

$$\begin{aligned}&\hat{\mathbf{u}}\cdot\tilde{\mathbf{N}}_n\left(k_x,k_y,z\right)=\frac{1}{k}\hat{\mathbf{u}}\cdot\mathbf{k}_\rho 4j^n e^{-jn\varphi_{\mathrm{G}}}\frac{\mathrm{d}}{\mathrm{dz}}\chi\left(z;\kappa_\rho\right)\\&\times\frac{\left[k_x-j\,\mathrm{sgn}(n)k_y\right]^{|n|}}{\kappa_\rho^{|n|}}\frac{1}{k_x^2+k_y^2-\kappa_\rho^2}\end{aligned}\quad(27)$$

as reported in (9).

REFERENCES

[1] T. Nguyen, H. Ueda, J. Hirokawa, and M. Ando, "A radial line slot antenna for an elliptical beam," *IEEE Trans. Antennas Propag.*, vol. 60, no. 12, pp. 5531–5537, Dec. 2012.

[2] M. Albani, A. Mazzinghi, and A. Freni, "Automatic design of CP-RLSA antennas," *IEEE Trans. Antennas Propag.*, vol. 60, no. 12, pp. 5538–5547, Dec. 2012.

[3] W. C. Chew, *Waves and Field in Inhomogeneous Media*. New York: IEEE Press, 1995.

[4] L. B. Felsen and N. Marcuvitz, *Radiation and Scattering of Waves*. IEEE Press, 1994.

[5] M. Albani, G. La Cono, R. Gardelli, and A. Freni, "An efficient full-wave method of moments analysis for RLSA antennas," *IEEE Trans. Antennas Propag.*, vol. 54, no. 8, pp. 2326–2336, Aug. 2006.

[6] T. S. Bird and D. G. Bateman, "Mutual coupling between rotated horns in a ground plane," *IEEE Trans. Antennas Propag.*, vol. 42, pp. 1000–1006, Jul. 1994.

[7] D. G. Bateman, T. S. Bird, and A. S. Mohan, "Asymptotic approximation of some integrals involved in EFIE solutions using the method of moments," *Proc. Inst. Elect. Eng. Microw., Antennas Propag.*, vol. 145, no. 4, pp. 361–365, Aug. 1998.

[8] M. Albani, A. Mazzinghi, and A. Freni, "Asymptotic approximation of mutual admittance involved in MoM analysis of RLSA antennas," *IEEE Trans. Antennas Propag.*, vol. 57, no. 4, pp. 1057–1063, Apr. 2009.

[9] G. O. Young, "Synthetic structure of industrial plastics (Book style with paper title and editor)," in *Plastics*, 2nd ed. vol. 3, J. Peters, Ed. New York: McGraw-Hill, 1964, pp. 15–64.

[10] D. Deslandes and K. Wu, "Integrated microstrip and rectangular waveguide in planar form," *IEEE Microw. Wirel. Comp. Lett.*, vol. 11, no. 2, pp. 68–70, Feb. 2001.

[11] D. Deslandes, M. Bozzi, P. Arcioni, and K. Wu, "Substrate integrated slab waveguide (SISW) for wideband microwave applications," in *Proc. IEEE MTT-S Int. Microwave Symp.*, vol. 2,, pp. 1103-1106, Jun. 2003.

[12] S. Park, Y. Okajima, J. Hirokawa, and M. Ando, "A slotted post-wall waveguide array with interdigital structure for 45° linear and dual polarization," *IEEE Trans. Antennas Propag.*, vol. 53, no. 9, pp. 2865–2871, Sep. 2005.

[13] M. Ettorre, R. Sauleau, and L. Le Coq, "Multi-beam multi-layer leaky wave SIW pillbox antenna for millimeter-wave applications," *IEEE Trans. Antennas Propag.*, vol. 59, no. 4, pp. 1093 – 1100, Apr. 2011.

[14] M. Ettorre, R. Sauleau, L. Le Coq, and F. Bodereau, "Single-folded leaky-wave antennas for automotive radars at 77 GHz," *IEEE Antennas Wireless Propag. Lett.*, vol. 9, pp. 859 - 862, 2010.

[15] E. Gandini, M. Ettorre, M. Casaletti, K. Tekkouk, L. Le Coq, and R. Sauleau, "SIW slotted waveguide array with pillbox transition for mechanical beam scanning," *IEEE Antennas Wireless Propag. Lett.*, vol. 11, pp. 1572–1575, 2012.

[16] M. Casaletti, R. Sauleau, M. Ettorre, and S. Maci, "Efficient analysis of metallic and dielectric posts in parallel-plate waveguide structures," *IEEE Trans. Microw. Theory Tech.*, vol. 60, no. 12, p.2979 – 2989, Oct. 2012.

[17] M. Casaletti, G. Valerio, J. Seljan, M. Ettorre, and R. Sauleau, "A full-wave hybrid method for the analysis of multilayered SIW-based antennas," *IEEE Trans. Antennas Propag.*, vol. 61, no. 11, Nov. 2013. doi:10.1109/TAP.2013.2279795.

[18] B. Wu and L. Tsang, "Signal integrity analysis of package and printed circuit board with multiple vias in substrate of layered dielectrics," *IEEE Trans. Adv. Pack.*, vol. 33, no. 2, pp. 510 – 516, May 2010.

[19] A. Quarteroni, R. Sacco, and F. Saleri, *Numerical Mathematics*. New York: Springer, 2000.

[20] I.S. Gradsteyn and I.M. Ryzhik, *Table of Integrals, Series, and Products*. 7th ed., Academic Press, Boston, 2007.